Competition between Fullerene Aggregation and Poly(3-hexylthiophene) Crystallization upon Annealing of Bulk Heterojunction Solar Cells

Wei-Ru Wu,[†] U-Ser Jeng,[†,*] Chun-Jen Su,[†,*] Kung-Hwa Wei,[‡] Ming-Shin Su,[‡] Mao-Yuan Chiu,[‡] Chun-Yu Chen,[†] Wen-Bin Su,[†] Chiu-Hun Su,[†] and An-Chung Su[§]

[†]National Synchrotron Radiation Research Center, 101 Hsin-Ann Road, Hsinchu Science Park, Hsinchu 30076, Taiwan, [‡]Department of Materials Science and Engineering, National Chiao Tung University, 1001 Ta Hsueh Road, Hsinchu 30050, Taiwan, and [§]Department of Chemical Engineering, National Tsing Hua University, Hsinchu 30013, Taiwan

ABSTRACT Concomitant development of [6,6]-phenyl-C_{61}-butyric acid methyl ester (PCBM) aggregation and poly(3-hexylthiophene) (P3HT) crystallization in bulk heterojunction (BHJ) thin-film (*ca.* 85 nm) solar cells has been revealed using simultaneous grazing-incidence small-/wide-angle X-ray scattering (GISAXS/GIWAXS). With enhanced time and spatial resolutions (5 s/frame; minimum $q \approx 0.004$ Å^{-1}), synchrotron GISAXS has captured in detail the fast growth in size of PCBM aggregates from 7 to 18 nm within 100 s of annealing at 150 °C. Simultaneously observed is the enhanced crystallization of P3HT into lamellae oriented mainly perpendicular but also parallel to the substrate. An Avrami analysis of the observed structural evolution indicates that the faster PCBM aggregation follows a diffusion-controlled growth process (confined by P3HT segmental motion), whereas the slower development of crystalline P3HT nanograins is characterized by constant nucleation rate (determined by the degree of supercooling and PCBM demixing). These two competing kinetics result in local phase separation with space-filling PCBM and P3HT nanodomains less than 20 nm in size when annealing temperature is kept below 180 °C. Accompanying the morphological development is the synchronized increase in electron and hole mobilities of the BHJ thin-film solar cells, revealing the sensitivity of the carrier transport of the device on the structural features of PCBM and P3HT nanodomains. Optimized structural parameters, including the aggregate size and mean spacing of the PCBM aggregates, are quantitatively correlated to the device performance; a comprehensive network structure of the optimized BHJ thin film is presented.

KEYWORDS: GISAXS · GIWAXS · structural kinetics · bulk heterojunction solar cells · charge mobility

Morphology of the active layer of bulk heterojunction (BHJ) thin films, comprising donor and acceptor components, is one of the critical factors in solar cell performance optimization.[1,2] An ideal morphology for BHJ thin-film solar cells features in phase-separated nanodomains *ca.* 10 nm in size to facilitate exciton dissociation and charge transport;[3] also relevant is the connectivity of these nanodomains in the respective phases for charge transport.[1−4] In the past decade, BHJ thin-film processing parameters, such as composition, annealing temperature/time, casting solvent, and film thickness, have been intensively studied. As a result, power conversion efficiency (PCE) in excess of 4% could be obtained with the popular BHJ blend of regioregular poly(3-hexylthiophene) (P3HT) and [6,6]-phenyl-C_{61}-butyric acid methyl ester (PCBM).[5−7] In general, optimized device performance of this BHJ blend can be achieved with films of PCBM/P3HT weight ratio c = 0.8−1.0 and *ca.* 100 nm in thickness after thermal annealing at 120−160 °C for 15−30 min; processing details determine that these parameters fluctuate in a certain range.[7]

In correlating performance and morphology, cross-sectional transmission electron microscopy (TEM)[3] and electron tomography[8] revealed mutually intercalated nanodomains of the two constituted components in the P3HT/PCBM thin-film solar cells; correspondingly, grazing-incidence X-ray diffraction (GIXRD) indicated highly oriented P3HT lamellae (*ca.* 10−20 nm in domain size), with chain stacking perpendicular to the film substrate.[5,9] Compared to the relatively well-elucidated structural characteristics of P3HT crystallites, PCBM aggregation behavior upon annealing in the composite film is much less clarified.[10,11] This situation is partly due to the fact that the commonly used tool of X-ray diffraction revealed very limited structural information of noncrystalline PCBM aggregates; because of the contrast, PCBM aggregates could be clearly identified by TEM after full crystallinity development upon extensive thermal treatment beyond optimized film processing conditions. As a result, the proposed PCBM aggregate size for optimized

* Address correspondence to usjeng@nsrrc.org.tw, su.cj@nsrrc.org.tw.

Received for review March 22, 2011 and accepted July 12, 2011.

Published online July 12, 2011
10.1021/nn2010816

© 2011 American Chemical Society

P3HT/PCBM thin-film solar cells scattered in a wide range of 5−60 nm.[9,12−14]

Very recently, structural kinetics of polymer/fullerene derivative thin films in thermal annealing has received increasingly more attention for better understanding of the local phase separation and nanodomain formation mechanism of the related solar cells. Using *in situ* GIXRD, Shin *et al.* showed that the P3HT crystallization process in a P3HT/PCBM blend was completed in 2−5 min during annealing at 140 °C.[15] Using the same methodology of *in situ* GIXRD, Verploegen *et al.* demonstrated that PCBM crystalline reflections slowly appeared within 20 min of annealing above 150 °C.[16] In contrast, *ex situ* small-angle neutron scattering (SANS) revealed a much faster morphology development for a similar film upon short-term thermal annealing of a few seconds.[13] Combining SANS, TEM, and GIXRD observations, Chen *et al.*[13] suggested that the phase separation length scale was incommensurate with spinodal decomposition for polymer mixtures and hence more likely a result of competition between P3HT crystallization and PCBM diffusion during thermal annealing: the ratio of PCBM diffusion coefficient to P3HT crystallization rate conceivably determined the limited P3HT crystal size during local phase separation that led to bicontinuous P3HT- and PCBM-rich nanodomains in the BHJ thin-film solar cell. Retrieving the fast PCBM aggregation kinetics before crystallization in such composite thin films, however, would require time-resolved (in seconds) grazing-incidence small-angle X-ray scattering (GISAXS) or SANS for large noncrystalline PCBM aggregates, which was not addressed in previous studies.

Basic understanding of the kinetics of PCBM aggregation and P3HT crystallization and their correlations in the morphological development of P3HT/PCBM composite films upon thermal annealing would provide hints to the optimal processing of future BHJ solar cells with varied components of fullerene derivatives or other conjugated polymers.[13] In this study, we employ simultaneous and time-resolved GISAXS and grazing-incidence wide-angle X-ray scattering (GIWAXS) to capture the kinetics of PCBM aggregation and P3HT crystallization in the corresponding BHJ thin films during *in situ* thermal annealing.[15,16] With improved time and spatial resolutions (5 s/frame; minimum scattering wavevector $q \approx 0.004$ Å^{-1}), synchronized GISAXS and GIWAXS have captured the concomitant growth of the PCBM aggregates (from 7 to 18 nm in size) and the P3HT crystallites (from 7 to 12 nm), within 100 s of annealing at 150 °C. We compare the growth kinetics of the nanodomains of the two components based on the Avrami exponents and rate constants extracted from the evolutions of the corresponding structural parameters. Parallel measurements on the hole and electron mobilities of the corresponding BHJ thin films under similar annealing conditions further demonstrate synchronized developments of charge mobility and nanodomain formation. Quantitative correlations drawn between the morphology and charge mobility are discussed in terms of the charge transport behavior and device performance of the BHJ solar cell.

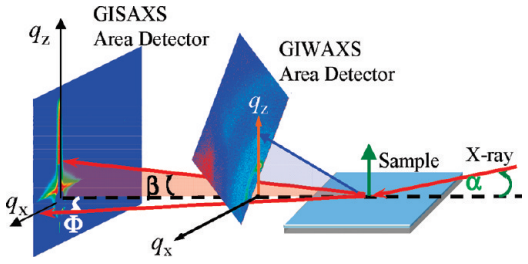

Figure 1. Schematic of the setup for synchronized GISAXS/GIWAXS, with the beam incident angle α and the scattering angles β and Φ in the out-of-plane (q_z) and in-plane directions (q_x). The GIWAXS detector plane was normal to the incident beam; the detector was titled 45° out of the horizontal plane to cover scattering in the q_z and q_x directions.

With the new approach of simultaneous/time-resolved GISAXS/GIWAXS and the structural analysis for kinetics parameters, we have made new findings centering on the critical aggregation behavior of PCBM in the P3HT−PCBM blend; these include (1) the thermal equilibrium aggregation sizes and the growth kinetics of PCBM, (2) faster PCBM aggregation kinetics than that for P3HT crystallization (opposite to previous speculations), (3) a deduced activation energy for PCBM aggregation that addresses the phase separation mechanism of P3HT and PCBM (for the interacted or bicontinuous P3HT and PCBM nanodomains) in more appropriate terms of nucleation and growth, rather than the spontaneous spinodal decomposition (requiring no activation energy) that has been suspected for some time, and (4) closely and quantitatively correlated PCBM aggregation size and electron mobility that has long been postulated. The present results not only clarify the mechanistic origins of morphological development in P3HT/PCBM films but also provide insights to the performance optimization of polymer/fullerene organic thin-film devices in general.

RESULTS AND DISCUSSION

Simultaneous GISAXS/GIWAXS. With the experimental setup shown in Figure 1, we could measure time-resolved GIWAXS and GISAXS patterns simultaneously for the P3HT/PCBM composite films (c = 1.0) *in situ* annealed at 150 °C (*cf.* movie in the Supporting Information). The GISAXS and GIWAXS patterns, representatively shown in Figure 2, exhibited concomitant and substantial changes during the heating process (*ca.* 40 s) from an ambient temperature to 150 °C; the scattering patterns were quickly saturated within the subsequent 100 s of isothermal annealing, revealing fast morphology development of the composite film. Specifically, the GIWAXS patterns evidenced successively enhanced P3HT lamellar peaks up to the third order (Figure 2a−e) in the vertical direction, corresponding

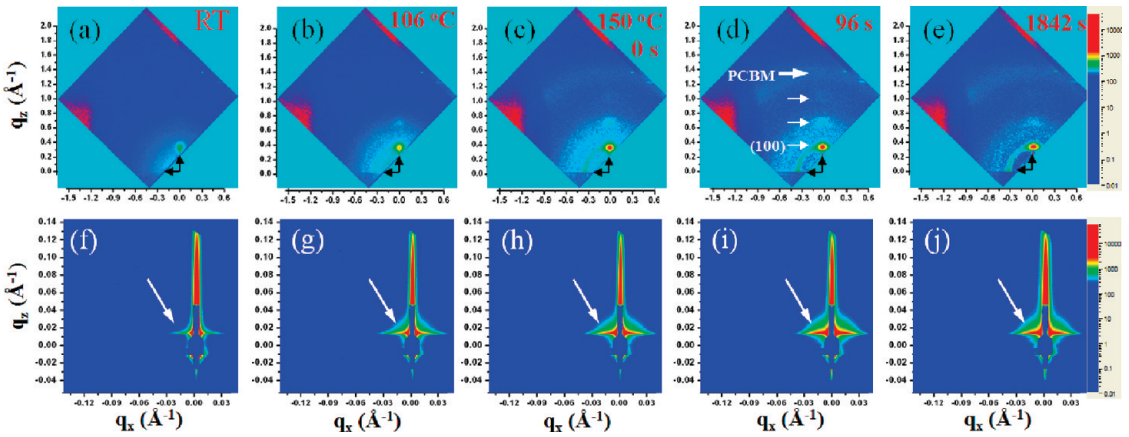

Figure 2. Representative five sets of the GIWAXS (top row) and GISAXS (bottom row) images simultaneously measured for the P3HT/PCBM film with c = 1.0. From left to right are the images collected (a) at room temperature, (b) during the heating process (106 °C), and (c−e) after 0, 96, and 1842 s of annealing at 150 °C. The lamellar peaks (100), (200), and (300) of the P3HT crystallites are marked in (d) by thin arrows, whereas the PCBM halo ($q \approx 1.4$ Å^{-1}) is indicated with a thick arrow. The arrows in the GISAXS patterns mark the successively enhanced scattering in the low-q_x region.

to edge-on P3HT lamellae with the lamellar stacking direction perpendicular to the substrate surface. The concomitant growth of the (100) peak in the in-plane direction (Figure 2a−e) corresponded to the development of face-on lamellae domains with the lamellar stacking oriented parallel to the film surface. Meanwhile, the emerged GIWAXS halo at $q \approx 1.4$ Å^{-1} during the annealing process revealed formation of a short-range packing of PCBM after aggregation.[9] The PCBM aggregates also resulted in prompt and drastic increase of scattering intensity in the low-q region (0.004−0.04 Å^{-1}) of the corresponding GISAXS patterns simultaneously observed. Note that scattering in the low-q region was mainly dominated by large PCBM aggregates as elucidated in our previous study.[10] During the subsequently prolonged annealing over 1800 s, both GISAXS and GIWAXS images changed marginally and resembled those measured for *ex situ* annealed (at 150 °C for 900 s) samples. With the time resolution of 5 s, these time-resolved GIWAXS/GISAXS data revealed rich structural information, especially the mutually confined growth kinetics of P3HT and PCBM nanodomains in the composite film as elucidated below.

Growth of PCBM Aggregates. Figure 3a presents the GISAXS profiles of the P3HT/PCBM (c = 1.0) film selectively extracted from the corresponding 2D patterns along the q_x direction (at the specular beam position $q_z \approx 0.018$ Å^{-1}),[17] revealing the fast scattering development in the low-q region 0.004−0.04 Å^{-1} within the first 60 s of thermal annealing. Furthermore, the selected GISAXS profiles (Figure 3c) for 60, 600, and 1800 s at 150 °C overlapped roughly, revealing quickly saturated PCBM aggregation. A broad interference shoulder at $q_x \approx 0.025$ Å^{-1} shaped during the annealing, corresponding to formation of a liquid-like or distorted face-centered-cubic-like packing of PCBM aggregates with a mean spacing of *ca.* 25 nm (detailed below with model fitting).[18] For comparison, the GISAXS profile similarly measured for a pristine P3HT film annealed at 150 °C for 1800 s contributed only marginally in this monitored q region, as illustrated in Figure 3c.

To obtain detailed structural evolution of the PCBM aggregates, we used the sphere form factor $P(q)$ with the Schultz size distribution for GISAXS data fitting.[14] An approximated structure factor $S(q)$ taken from the effective one-component system of hard spheres was also included in the data fitting to account for the scattering shoulder around $q_x \approx 0.025$ Å^{-1} from loosely packed PCBM aggregates. Illustrated in Figure 3a are the decent data fitting results. Note that the form factor of ellipsoids or rods could not fit the GISAXS data, as well. Hence, we focus on the structural information, especially the size evolution, given by the model of polydisperse spheres. Shown in Figure 3b,d are the size distributions (in general, 20−30%) and the size evolution during annealing, indicating that PCBM aggregates grew slightly from a diameter of *ca.* 7 nm (as-cast film) to 10 nm during heating toward 150 °C. In the subsequent 60 s of isothermal annealing, the PCBM aggregate size increased quickly from 10 to 17.5 nm, then remained about the same in the prolonged thermal annealing over 1800 s. In all of the GISAXS data fitting, we had to include a scattering term described by the Debye−Buche correlation function,[19] $I(q_x) = (1 + q_x^2\zeta^2)^{-2}$, to account for the relatively sharp upturn scattering in the very low-q region 0.004−0.007 Å^{-1}. The fitted values for the Debye−Buche correlation length ζ were about the same (60 ± 10 nm) for all sets of data; hence, the structural origin of this correlation length might be irrelevant to PCBM aggregation. Possibly, the correlation length might associate better with the reported P3HT aggregates of nanowhisker or protofibril structure already formed in solutions.[20] Using a model of polydisperse rods,[21] with a mean rod length of 69 nm, a rod diameter of 11.2 nm, and 75% polydispersity in rod length, we could fit decently the

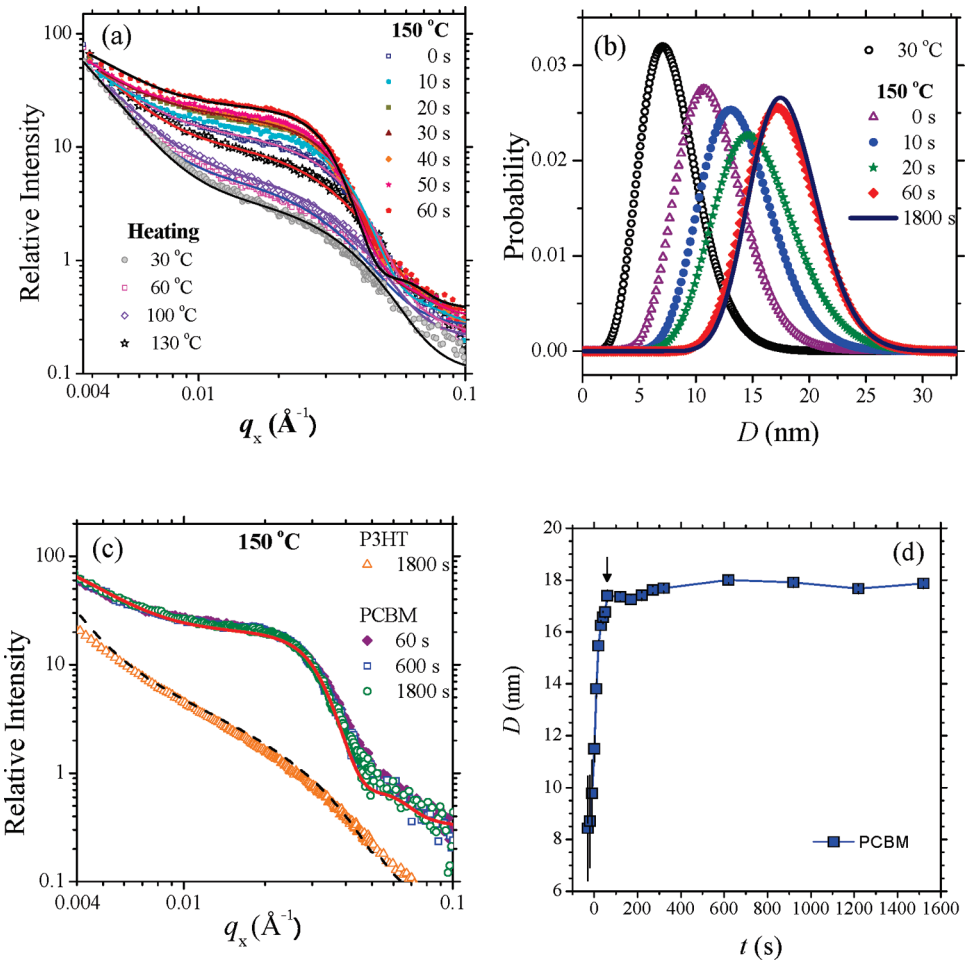

Figure 3. (a) Selected GISAXS profiles measured for the P3HT/PCBM film (c = 1.0) during the heating process to 150 °C and the subsequent isothermal annealing within 60 s. The data are fitted (solid curves) using polydisperse spheres with the Schultz size distributions shown in (b). (c) Approximately overlapped GISAXS data collected after 60, 600, and 1800 s of thermal annealing. The data for 1800 s are fitted (solid curve) with the size distribution shown in (b). For comparison, the GISAXS data for a pristine P3HT film annealed at 150 °C for 1800 s are also shown; the data are fitted (dashed curve) with polydisperse (in rod length) rods. (d). Corresponding mean size (D) evolution of PCBM aggregates.

GISAXS profile of the pristine P3HT annealed at 150 °C (Figure 3c). These results suggest that P3HT forms/enhances lamellar stacking within the fibril-like aggregates upon thermal annealing, as to be delineated below.

Growth Behavior of P3HT Crystallites. Respectively shown in Figure 4a,b are the evolutions of the two P3HT (100) peaks for the edge-on and face-on lamellae of the P3HT/PCBM blend film (c = 1.0) during 150 °C annealing. These profiles were extracted from the corresponding GIWAXS patterns along the normal-to-plane (q_z) and in-plane (q_x) directions. During the heating process to 150 °C, the two (100) peaks sharpened concomitantly and shifted successively from q_z = 0.388 to 0.355 Å^{-1} owing largely to thermal expansion of the lamellae; the peaks could shift back closely to 0.374 Å^{-1} when the sample was cooled to ambient temperature after thermal annealing, as also observed for a pristine P3HT film in a similar annealing process. After the thermal annealing, the enhanced orientation of P3HT lamellae along the surface normal direction, however, revealed straightened lamellar stacking with a slightly larger lamellar spacing of 16.8 Å than that (16.2 Å) before annealing.[15] Using the Scherrer's equation,[10] we could obtain the lamellar domain size evolution from the corresponding (100) peak widths. The growth behaviors shown in Figure 4c indicate that the P3HT edge-on and face-on lamellae developed with comparably fast kinetics and were largely saturated within the first 100 s of 150 °C thermal annealing. The slightly larger domain size of 14.5 nm for the face-on lamellae than that (11.5 nm) for the edge-on lamellae is consistent with that shown in a previous study;[15] the edge-on lamellae, however, dominated the P3HT crystallinity development in the composite film, as revealed by their much higher (100) peak intensity (by 8-fold) as compared to that of the face-on lamellae (*cf.* Figure S1 in Supporting Information).

Formation Mechanism of the Nanograins. To better understand the growth behavior of the PCBM aggregates and P3HT crystallites from the structural evolutions

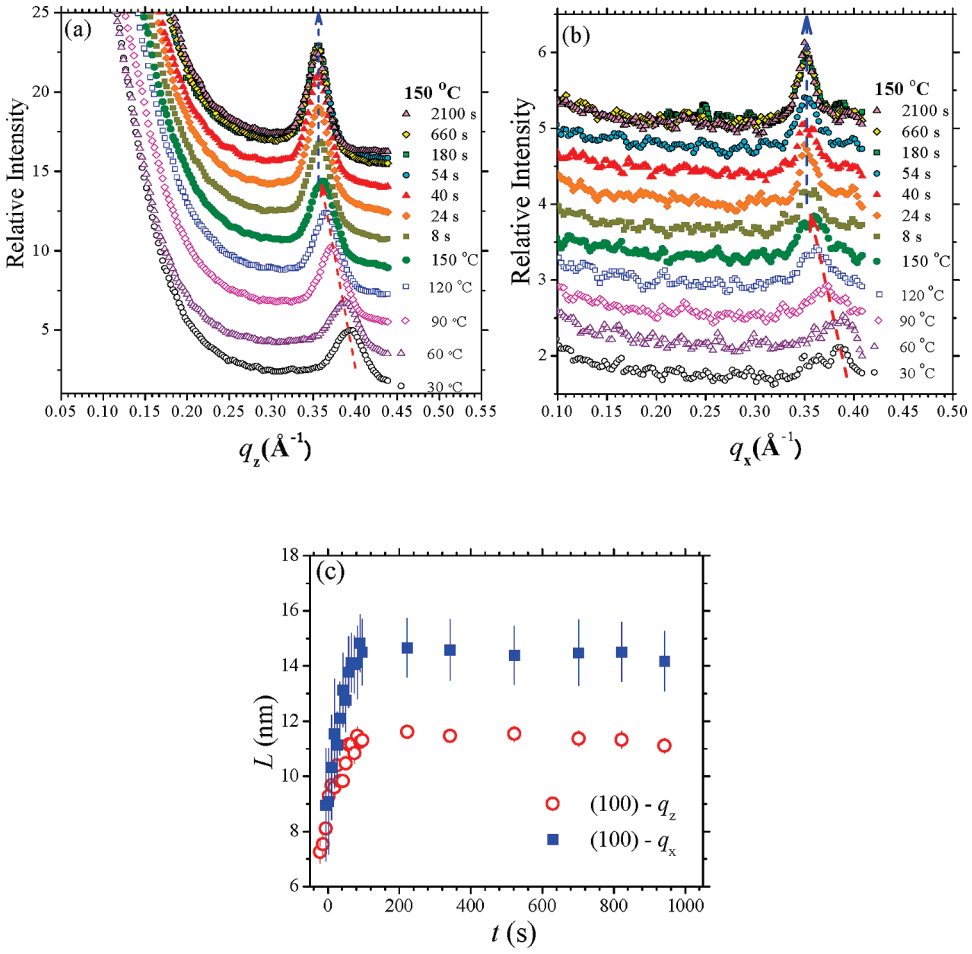

Figure 4. Evolutions of the P3HT (100) peak in the (a) normal-to-plane q_z and (b) in-plane q_x directions extracted from the corresponding GIWAXS images for the P3HT/PCBM (c = 1.0) blend film during 150 °C annealing. The profiles are shifted vertically in intensity for clarity. (c) Corresponding size evolutions of the respective lamellar domains in the two perpendicular orientations.

revealed by the time-resolved GISAXS/GIWAXS data, we adopted the Avrami–Erofeev expression[22,23]

$$\alpha(t) = 1 - \exp[-(kt)^n] \quad (1)$$

where the extent of the phase volume development $\alpha(t)$ at time t was characterized by the Avrami exponent n and rate constant k, assuming no induction time in the system. For PCBM aggregation kinetics, $\alpha(t)$ was taken from the scattering invariant $Q_{inv} = \int I(q)q^2dq$ in the GISAXS q region where PCBM aggregates dominated the scattering contribution. For P3HT crystallization kinetics, $\alpha(t)$ was deduced from the integrated intensity of the (100) peak $I_{100}(t)$ normalized by its maximum (saturated) value. Shown in Figure 5 are the obtained $\alpha(t)$ evolutions for the PCBM aggregation and the P3HT crystallization (edge-on and face-on lamellae, respectively) of the P3HT/PCBM (c = 1.0) composite film (*cf.* Figures 3 and 4). These $\alpha(t)$ profiles could be fitted reasonably well (Figure 5a) using eq 1, with the best-fitted n and k values listed in Table 1, or presented graphically using the Sharp–Hancock form[23]

$$\ln\{\ln[1-\alpha(t)]^{-1}\} = n\ln t + n\ln k \quad (2)$$

as given in Figure 5b.

As shown in Table 1, PCBM aggregation and P3HT crystallization have similar Avrami exponents of $n \approx 1$. Nevertheless, since the Avrami exponent n is contributed by both primary nucleation and growth, formation mechanisms of the two types of nanodomains in the composite film may not necessarily be the same.[24,25] In view of the quick growth ($D \propto t^{0.3}$) of the PCBM aggregates illustrated in Figure 3d, we neglected the nucleation factor and attributed the $n \approx 1$ value largely to a three-dimensional growth ($D^3 \propto t^{0.9}$) of PCBM aggregates in the BHJ thin film.[24,25] Indeed, isotropic, diffusion-controlled type of growth fits adequately the local demixing process of PCBM from the well-dispersed P3HT/PCBM background. For ideal diffusion-limited aggregation of existing particles, phase dimension grows with $D \propto t^{1/2}$ and the corresponding Avrami exponent contributed by size growth alone is presumably $n = d/2$, where d is the Euclidean dimension between 1 and 3.[25] The smaller growth exponent to the annealing time ($D \propto t^{0.3}$) of PCBM aggregation than that for the ideal diffusion-limited growth process might be attributed to more restricted, heterogeneous diffusion routes out of the mixed phase.[24]

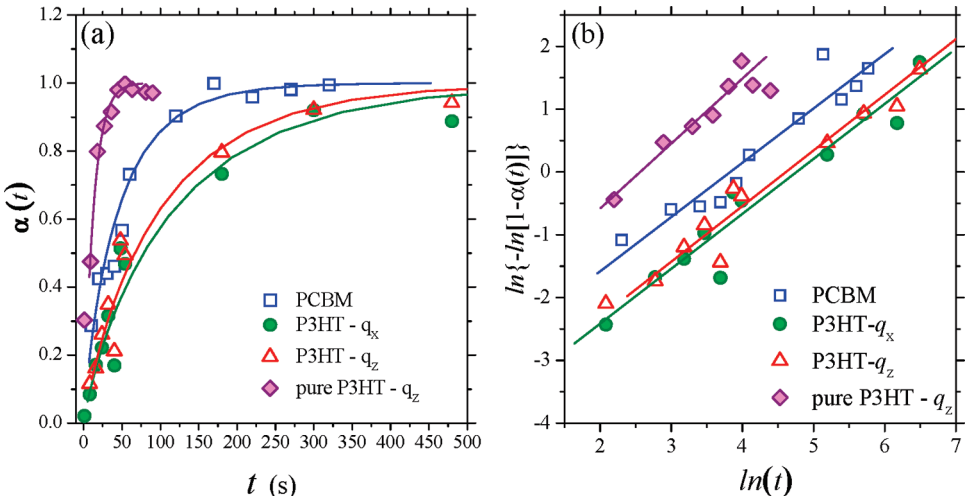

Figure 5. (a) Values of α(*t*) for PCBM aggregation and P3HT crystallization (edge-on and face-on lamellae along q_z and q_x, respectively) of the composite film with *c* = 1.0, at 150 °C annealing. Also shown is the α(*t*) for the edge-on lamellae in a pristine P3HT film *in situ* annealed similarly. The data are fitted (solid curves) using eq 1. (b) Corresponding Sharp–Hancock presentations of the data, linearly fitted (solid lines) using the Avrami exponents (slopes) and rate constants listed in Table 1.

TABLE 1. Best-Fit Values of the Avrami Exponents *n* and Rate Constants *k* of PCBM Aggregation and P3HT Crystallization for the Edge-On and Face-On Lamellae in the Composite Film of PCBM/P3HT with *c* = 1.0 at 150 °C (Also Shown Are the Kinetics Parameters for a Pristine P3HT Film Similarly Annealed)

	PCBM aggregates	P3HT face-on lamellae	P3HT edge-on lamellae	pure P3HT edge-on lamellae
n	0.9 ± 0.1	0.9 ± 0.1	0.9 ± 0.1	1.0 ± 0.1
k (s^{-1})	0.036 ± 0.015	0.017 ± 0.009	0.016 ± 0.006	0.071 ± 0.030

In contrast, the size growth of P3HT crystallites ($L \propto t^{0.06}$) extracted from the data measured during the 150 °C annealing (Figure 4c) was more strongly hindered, especially for the predominating edge-on lamellae. Hence, we attribute the Avrami exponent $n \approx 1$ obtained mainly as a result of constant nucleation rate of crystalline P3HT nanograins in the composite film.[24,25]

Despite the similar Avrami exponent of $n \approx 1$, PCBM aggregation kinetics exhibited a significantly higher Avrami rate constant of $k = 0.036\ s^{-1}$ (Table 1) than those of P3HT crystallization for edge-on ($k = 0.017\ s^{-1}$ along the film normal direction) and face-on lamellae ($k = 0.016\ s^{-1}$ along the film surface direction). It should be emphasized that the kinetics detailed here for PCBM *aggregation* is much faster than that reported for PCBM *crystallization*.[16] In the absence of PCBM, crystallization in a pristine P3HT film annealed at 150 °C (Figure 5) exhibited a 4-fold higher rate constant of $k = 0.071\ s^{-1}$ for the edge-on P3HT lamellae (Table 1) and a similar Avrami exponent of $n = 1$ as that for the P3HT lamellae in the composite film. These results suggest that the presence of PCBM molecules seriously hinders the nucleation rate (in terms of *k*) of P3HT lamellae but does not change the basic scheme of nucleation-controlled crystallization (in terms of $n \approx 1$, *i.e.*, constant nucleation rate) in the P3HT-rich region upon segregation. Aggregates formed by densely segregated PCBM molecules then serve to confine the growth space and orientation of P3HT, leading to better aligned (space-filling) P3HT lamellae than that in the pristine P3HT film, as revealed from the significantly sharpened (100) peak of the composite film (*cf.* Figure S1). The concurrent/consequential development of P3HT crystalline domains upon PCBM segregation then serve in turn to confine further development of PCBM aggregates. The competition between the mutually interacting growth mechanisms, rather than spinodal decomposition,[13,26] of the two components leads to concomitant saturation (*cf.* Figures 3d and 4c) at mutually limited nanodomain sizes below *ca.* 20 nm.

We also conducted GISAXS/GIWAXS for the composite films isothermally annealed at different temperatures. It was found that the rate constant of PCBM aggregation increased strongly from $k = 0.014\ s^{-1}$ at 120 °C to $0.036\ s^{-1}$ at 150 °C, whereas the *k* value for P3HT lamellae grew moderately from $0.009\ s^{-1}$ at 120 °C to $0.016\ s^{-1}$ at 150 °C (Supporting Information Figure S2). From the three Avrami rate constants for PCBM aggregation at 120, 150, and 160 °C, we could extract an activation energy of $E_a = 64.0 \pm 12.3$ kJ/mol (15.3 ± 3.0 kcal/mol) for PCBM aggregation from the Arrhenius plot[25] in Figure 6. Interestingly, the E_a value for PCBM aggregation is close to the barrier of ~15 kcal/mol theoretically calculated for rotation of neighboring thiophene rings from coplanar to orthogonal conformations (related to the coil-to-rod transformation)[27] along the regioregular poly(3-propylthiophene) (P3PT) backbone. This E_a value, however, is significantly smaller than the activation energy 37.5 kcal/mol for P3HT crystallization.[27] These observations suggest that chain motion of P3HT controls the diffusion and aggregation of PCBM, but its own (nucleation-dominated)

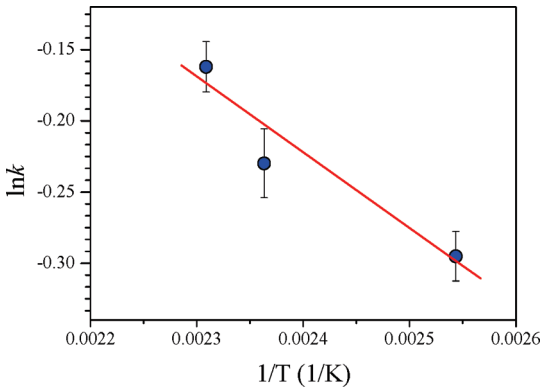

Figure 6. Arrhenius plot for the temperature-dependent Avrami rate constant *k* measured at 120, 150, and 160 °C for PCBM aggregation. The activation energy of PCBM aggregation can be obtained from the slope ($-E_a/R$) of the fitted line.

TABLE 2. Structural Parameters Extracted for the *In Situ* Annealed P3HT/PCBM Thin Films (*c* = 1.0; PCBM Volume Fraction ϕ_o = 41 vol %), Including the Edge-On Lamellar Domain Size *L* of P3HT Crystallites and the Size *D*, Mean Distance between Aggregates *d*, Wall-to-Wall Distance Δ (=*d* − *D*), Polydispersity *p*, and Surface-to-Volume Ratio *S*/*V* of the PCBM Aggregates, Together with the *D*/*L* Value[a]

c = 1.0 (41 vol %)	*L* (nm)	*D* (nm)	*d* (nm)	Δ (nm)	*P* (%)	ϕ (%)	ϕ_m (%)	*S*/*V* (nm^{-1})	*D*/*L*
as-cast	7.5	7.9	*b*	*b*	33	*b*		0.76	1.1
120 °C	9.6	13.2	18.8	5.6	44	18	23	0.45	1.4
150 °C	11.5	17.4	24.0	6.6	25	20	21	0.34	1.5

[a] The PCBM volume fraction in aggregation is ϕ (fitted based on the hard sphere structure factor) and that in the mixing phase ϕ_m (=$\phi_o - \phi$) with P3HT. [b] Information could not be determined.

crystallization is controlled by, most reasonably, the supercooling from its equilibrium melting temperature) after PCBM demixed. The mutually confined growths of PCBM aggregates and P3HT crystallites may therefore be modulated by the choice of annealing temperature. Segregation and subsequent aggregation of PCBM are expectedly better allowed at higher temperatures, leading to more efficiently increased (but not overgrown) PCBM aggregate size (*D*) and P3HT lamellar domain size (*L*), as indeed observed and summarized in Tables 2 and 3.

We have also conducted temperature-dependent GISAXS for a P3HT/PCBM composite film (*c* = 0.6) at successively elevated temperature from 30 to 180 °C (in 10 °C increments) with annealing time of 600 s for each temperature. Results shown in Figure 7a indicate gradual but identifiable increases of the PCBM aggregate size (*ca.* 8 nm in the as-cast state) at annealing temperatures above 100 °C (close to the glass transition temperature T_g of PCBM reported previously[16]) to *ca.* 16 nm at 170 °C. Upon further annealing at 180 °C, however, there is a stronger increase of the PCBM aggregation size to *ca.* 20 nm, as also evidenced by atomic force microscopic (AFM) images in Figure 7c. This sharper increase may be attributed to the reorganization (partial melting and recrystallization) of P3HT lamellae as the melting temperature of P3HT (*ca.* 195 °C)[16] is approached, which results in the relaxation of confinement on PCBM aggregates. This is supported by the emergence of the crystalline reflection at q_z = 1.37 $Å^{-1}$ from the broad halo of PCBM aggregates (Supporting Information Figure S3). On the other hand, GISAXS results for the P3HT/PCBM films with varied PCBM concentrations of *c* = 0.6, 0.8, and 1.0 revealed that the PCBM aggregate size (17.5 ± 1.0 nm) after annealing at the same temperature of 150 °C was independent of the PCBM concentration. We also notice that a certain fraction of PCBM molecules remain in the mixed phase in an optimized structure (*cf.* Tables 2 and 3). All of the present GISAXS results (as summarized in Tables 2 and 3 and Table S1 in Supporting Information) indicate that, within the studied composition and temperature ranges, PCBM aggregation size is determined mainly by kinetics of structural evolution.

Morphology−Charge Mobility Correlation. To correlate the morphological development of the P3HT/PCBM thin films to the corresponding solar cell performance, we have further monitored the changes of electron and hole mobilities for a BHJ film with *c* = 1.0 during annealing at 150 °C. Shown in Figure 8a is the uprising electron mobility, μ_e, observed within the first 100 s of thermal annealing, which becomes saturated subsequently. This synchronizes well with the development of $\alpha(t)$ for the PCBM aggregation (Figure 8a). Similarly observed is the accompanied development of the hole mobility, μ_h, that saturated slightly later than the electron mobility (Figure 8b). Correspondingly, the development of hole mobility synchronized with the $\alpha(t)$ for the development of P3HT lamellae, as illustrated in Figure 8b. These sensitive responses indicate that charge mobilities in the BHJ solar cell and consequently the short-circuit current density J_{sc} depend strongly on the developments of the P3HT and PCBM nanodomains upon heat treatment, whereas the increase of optical absorption owing to enhanced P3HT crystallization observed previously contributes only partly to J_{sc}.[14,28] Note that the values of the electron and hole mobilities obtained might be subject to device preparation conditions to some extent, and we believe that the relative values, hence the growth trends, of the charge mobilities shown in Figure 8 should be reliable.[9,29] In Table 3, the bulk structural characteristics extracted from GISAXS/GIWAXS for the P3HT/PCBM thin-film solar cells annealed at various temperatures are correlated to the corresponding device performance parameters extracted, with the corresponding current density−voltage curves shown in Supporting Information (Figure S4); accordingly, a cartoon in Figure 9 depicts the morphological features.

TABLE 3. Structural Parameters Extracted for the P3HT/PCBM (c = 0.8 or ϕ_o = 35%) Thin Films Annealed at 120, 150, and 180 °C for 900 s[a]

c = 0.8 (35 vol %)	L (nm)	D (nm)	d (nm)	Δ (nm)	p (%)	ϕ (%)	ϕ_m (%)	S/V (nm^{-1})	D/L	J_{sc} (mA/cm^2)	V_{oc} (V)	FF (%)	η (%)
as-cast	7.7	8.3	*b*	*b*	31	5	30	0.72	1.1	6.2	0.34	35	0.9
120 °C	10.8	13.8	20.9	7.1	20	15	20	0.43	1.3	8.7	0.47	55	2.8
150 °C	11.8	17.6	24.7	7.1	23	19	16	0.34	1.5	9.5	0.62	59	4.4
180 °C	15.9	19.4	26.7	7.3	44	20	15	0.31	1.2	8.7	0.66	53	3.8

[a] The notations for the structure parameters are the same as those in Table 2. The corresponding device performance parameters are short-circuit current density J_{sc}, open-circuit voltage V_{oc}, fill factor FF, and power conversion efficiency η. [b] Information could not be determined.

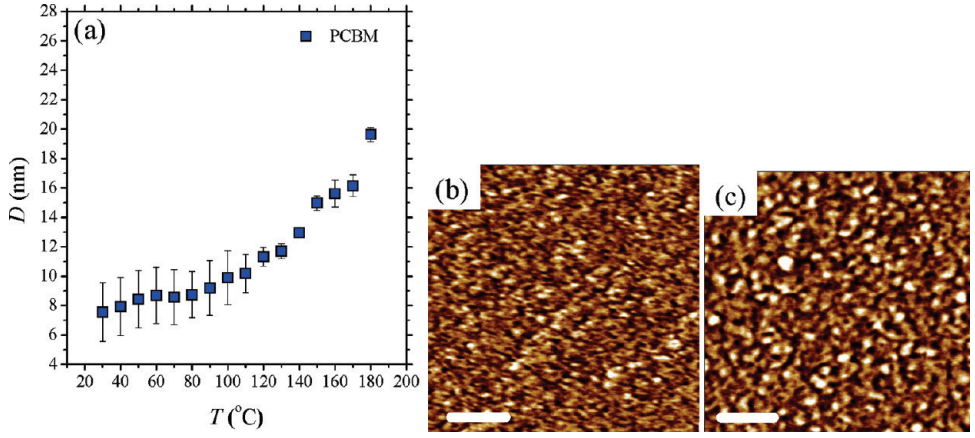

Figure 7. (a) GISAXS revealed growth of PCBM aggregates with the annealing temperature for a P3HT/PCBM composite film with c = 0.6. (b,c) Phase contrast AFM images of the P3HT/PCBM films annealed, respectively, at 150 and 180 °C for 900 s. The scale bars correspond to 200 nm.

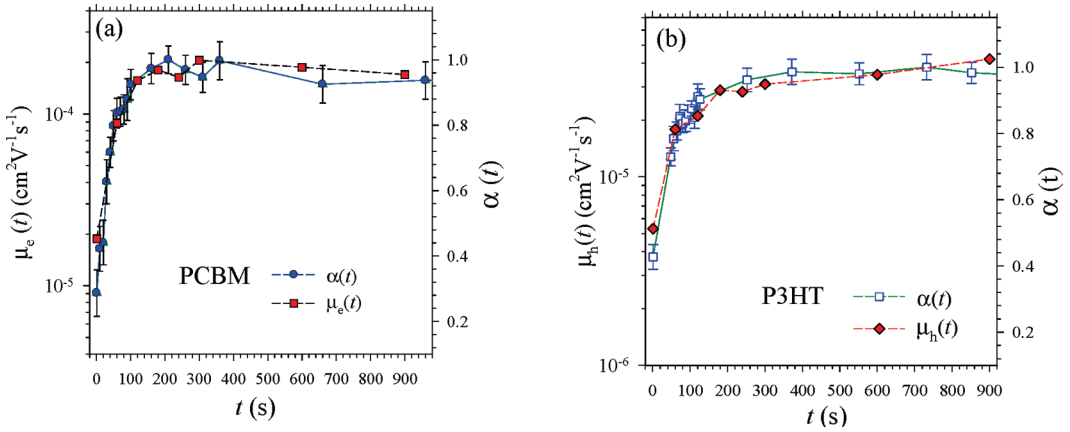

Figure 8. Strongly correlated developments of (a) the electron mobility and α(t) of PCBM aggregation, and (b) the hole mobility and α(t) of P3HT lamellae, of P3HT/PCBM composite films (c = 1.0) at 150 °C annealing.

Interestingly, the structure model is very much in line with the predictions based on the temperature–composition phase diagram of the binary P3HT–PCBM blend previously given by Kim and Frisbie,[30] in that below 200 °C and within the concentration range of ~30–50 wt % (or c = 0.5–1.0), PCBM is expected to dissolve in P3HT, in the form of dispersed molecules or noncrystalline aggregates, forming a metastable phase.

Note that the power conversion efficiency of a BHJ thin-film solar cell is collectively determined by many factors, although the bulk morphology of the BHJ films featured by intercalated nanograins is shown here to play a critical role on charge mobility, hence, J_{sc}. In view of the fast kinetics and fast saturation of the bulk morphology, the reported slight improvement of the P3HT/PCBM solar cell efficiency upon prolonged thermal annealing over several hundred seconds may associate more with surface/interface morphological features revealed by neutron reflectivity[31,32] or the slower interdiffusion behavior of P3HT/PCBM in the film in-depth direction.[33] Presumably, interfacial structures have slower thermal responses (kinetics) because

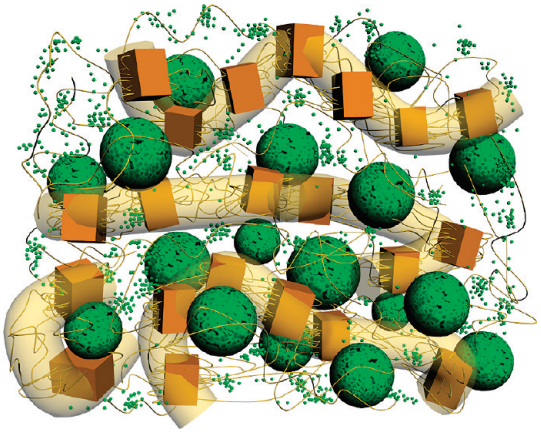

Figure 9. Cartoon for a thermally annealed P3HT/PCBM film, according to the structure characteristics shown in Table 3 (150 °C case). The intercalated PCBM aggregates (large spheres) and P3HT crystallites (blocks) are immersed in the matrix of P3HT amorphous chains (thin wires) and dispersed PCBM molecules (small spheres).

of larger substrate/surface restrictions or confinements. The quantitative correlation between charge mobility and film morphology established here may serve as a valuable reference in improving the algorithms and/or input parameters used in Monte Carlo model simulations of charge transport behavior.[4,34] Previously, in correlating hole mobility to film morphology for a conjugate MEH−PPV film, we have adopted the Gaussian disorder model (GDM) for the description of charge transport in organic semiconductors.[35] In GDM, charge mobility is modeled by two structure-related parameters, energy disorder σ and position disorder Σ, describing respectively, the spread of energy levels associated with charge transport and the fluctuations of intersite distance, thus the dispersion of site coupling.[36] Given the detailed structural information obtained here, it would be interesting to draw physical correlations between the disorder parameters σ (*via* a proper combination of molecular dynamics and quantum mechanical calculations)[37,38] and Σ to the structural information extracted, including the loosely packed nanograins (*ca.* 18 nm) of PCBM aggregates with a mean spacing of *ca.* 20−25 nm, the orientation preference and lamellar crystalline size (*ca.* 12−15 nm) of P3HT, and the volume fractions of respective phases. This, however, awaits further efforts in the near future.

Very recently, a related study[39] of the same material system focusing on a fixed annealing temperature of 140 °C up to *ca.* 1 h came to our notice. Combining real-time GIWAXS/ellipsometry/carrier mobility measurements during annealing and results of room-temperature device performance, Agostinelli *et al.*[39] have demonstrated that the microstructural evolution in P3HT/PCBM thin films involves two stages: in the first 5 min duration, crystallization of P3HT correlates with a major increase of photocurrent, which is followed by postulated aggregation of PCBM with increasing compactness upon which device performance remained unchanged. The present GISAXS/GIWAXS results encompass a broader temperature range (from 120 to 180 °C), additional details in the PCBM aggregation process, and thorough kinetic analysis of the morphological evolution during the early stage (the first 100 s) of annealing during which the device performance is improved most significantly. We demonstrate that it is the *competition* between crystallization of P3HT nanograins and aggregation of PCBM that dictates the morphological development and hence the device performance. The two studies are, nevertheless, complementary in certain aspects.

CONCLUSIONS

With synchronized GIWAXS and GISAXS of enhanced spatial/time resolutions, we have captured the competing kinetics of PCBM aggregation and P3HT crystallization of the corresponding BHJ thin-film solar cells. Within the first 100 s of thermal annealing at 150 °C, PCBM aggregation size in the P3HT/PCBM composite films grew quickly from 7 to 18 nm then saturated; meanwhile, the majority P3HT lamellae increased from a size of 7 to 12 nm. Both the kinetics of PCBM aggregation and P3HT crystallization could be characterized by similar Avrami exponents close to unity; the faster PCBM aggregation, however, has a 2-fold higher Avrami rate constant. The mutually confined growths led to comparable nanograin sizes of PCBM and P3HT below 20 nm, when annealing temperature was kept below 180 °C. The developments of PCBM and P3HT nanodomains could influence strongly and sensitively the electron and hole mobilities of the BHJ thin-film solar cells. The illustrated kinetics of structural evolution and its correlation to changes in charge mobility of P3HT/PCBM composite films may bear relevance to the selection of alternative polymer/fullerene derivative combinations and in the optimization of processing conditions for future BHJ thin-film solar cells.

EXPERIMENTAL METHODS

Regioregular P3HT (M_w = 35 kDa; received from Rieke Metals) was dissolved in chlorobenzene (15 mg L^{-1}) and mixed with a chlorobenzene solution (12 mg L^{-1}) of PCBM (Nano-C, Inc.) for different PCBM/P3HT weight ratios of c = 0, 0.6, 0.8, and 1.0; the corresponding PCBM volume fractions were 0, 29, 35, and 41%, respectively. Thin films (*ca.* 85 nm in thickness, characterized using X-ray reflectivity) were spun-cast from the mixtures onto Si wafers of dimensions of 2.0 cm × 2.0 cm and dried subsequently at ambient temperatures under N_2 gas flow.

Simultaneous GISAXS/GIWAXS measurements were performed at the BL23A endstation of the National Synchrotron Radiation Research Center (NSRRC), Taiwan. Details of the

instrument were reported previously.[40] Sample thin films were placed horizontally on a hot stage enclosed in an airtight chamber with thin (8 μm) Kapton windows for X-rays. To reduce sample degradation over prolonged irradiation more than 1800 s at 150 °C annealing, the sample chamber was evacuated then purged with N_2 gas. With a heating rate of 4 °C/s, sample temperature could reach 150 °C within 40 s. With an 8 keV (wavelength $\lambda = 1.550$ Å) beam and an incident angle 0.2°, time-resolved (5 s/frame), simultaneous GISAXS/GIWAXS were conducted using two area detectors triggered by the same signals for synchronized data collection. The detector system included (*i*) a CMOS flat panel X-ray detector C9728DK (52.8 mm square)[41] situated 7.2 cm from the sample position for GIWAXS, covering the first three diffraction peaks of P3HT lamellar crystallites, and (*ii*) a MAR165 CCD detector (165 mm in diameter), 300 cm from the sample position, allowing GISAXS data collection in the q region from 0.004 to 0.15 Å^{-1}. The scattering wavevector, defined as $q = 4\pi\lambda^{-1} \sin\theta$ (with 2θ the scattering angle), was calibrated using silver behenate, sodalite, and silicon powders, respectively.[40] GISAXS/GIWAXS profiles were extracted from the respective 2D patterns along q_x (with q_z fixed at the specular beam position)[42] and q_z in the in-plane and out-of-plane scattering directions, respectively, as illustrated in Figure 1. Experimental reproducibility was generally confirmed by repeated runs using fresh specimens.

For parallel measurements of charge mobility, hole-only devices were fabricated by spin-coating (600 rpm, 60 s) the same P3HT/PCBM mixture with $c = 1.0$ on top of the precoated PEDOT/PSS (Clevios PVP AI4083) layer (*ca.* 20 nm) of ITO substrates. Subsequently, a Au electrode (*ca.* 100 nm) was deposited on the P3HT/PCBM layer under high vacuum (*ca.* 10^{-7} Torr). Similarly, electron-only devices were fabricated by spin-coating an active layer of P3HT/PCBM ($c = 1.0$) on top of glass/Al (*ca.* 100 nm) substrates, followed by Ag evaporation (*ca.* 100 nm) for the top electrode. The thickness of each deposited layer was monitored using Veeco Dektak 150 surface profile meter. These hole-only and electron-only devices, eight samples for each type, were annealed at 150 °C for different lengths of time ranging from 60 to 900 s and measured subsequently at ambient temperature for characteristic responses of current density to the applied voltage. Electron or hole mobility was deduced from the measured current density based on the space charge-limited current model.[43,44]

Data Analysis. *GISAXS* intensity profiles in the lower-q region contributed by PCBM aggregates were modeled by polydisperse spheres using

$$I(q) = \langle n_p \rangle \langle P(q) \rangle S(q) \quad (3)$$

with the averaged form factor $\langle P(q) \rangle$ and structure factor $S(q)$.[45] The number density of the scattering particles $n_p(r) = \langle n_p \rangle f(r)$ is defined by the mean number density $\langle n_p \rangle$ and the Schultz size distribution function[46]

$$f(r) = \left(\frac{z+1}{r_a}\right)^{z+1} r^z \exp\left[-\left(\frac{z+1}{r_a}\right) r\right] / \Gamma(z+1), z > -1 \quad (4)$$

with the mean radius r_a, width parameter z, and polydispersity $p = (z+1)^{-1/2}$. The form factor for spheres $P(q) = [3j_1(qr)/(qr)]^2$ is defined by the first-order spherical Bessel function $j_1(qr)$. For spheres with small polydispersity, $S(q)$ may be approximated by the structure factor of the effective one-component system[45] of hard spheres

$$S(q) = [1 - n_p C(q)]^{-1} \quad (5)$$

with the effective diameter σ and volume fraction ϕ.[47,48] Here, $C(q) = 4\pi\sigma^3\xi^{-6}\{\alpha_o\xi^3(\sin\xi - \xi\cos\xi) + \beta_o\xi^2[2\xi\sin\xi - (\xi^2 - 2)\cos\xi - 2] + \gamma[(4\xi^3 - 24\xi)\sin\xi - (\xi^4 - 12\xi + 24)\cos\xi + 24]\}$ is defined by $\xi = q\sigma$, $\alpha_o = (1 + 2\phi)^2(1 - \phi)^{-4}$, $\beta_o = -6\phi[1 + (\phi/2)]^2(1 - \phi)^{-4}$, and $\gamma = \phi\alpha_o/2$.

Acknowledgment. We thank Dr. N. Yagi for the help in installation of the flat panel X-ray detector, and the National Science Council for financial support (NSC 99-2112-M-213-002-MY3).

Supporting Information Available: Simultaneous GISAXS/GIWAXS movie, GIWAXS data, kinetics analysis for 120 °C data, current density–voltage curves, structural parameters for the film with $c = 0.6$. This material is available free of charge *via* the Internet at http://pubs.acs.org.

REFERENCES AND NOTES

1. Frost, J. M.; Cheynis, F.; Tuladhar, S. M.; Nelson, J. Influence of Polymer-Blend Morphology on Charge Transport and Photocurrent Generation in Ddonor–Acceptor Polymer Blends. *Nano Lett.* **2006**, *6*, 1674–1681.
2. Yang, X.; Loos, J. Toward High-Performance Polymer Solar Cells: The Importance of Morphology Control. *Macromolecules* **2007**, *40*, 1353–1362.
3. Moon, J. S.; Lee, J. K.; Cho, S.; Byun, J.; Heeger, A. J. "Column-like" Structure of the Cross-Sectional Morphology of Bulk Heterojunction Materials. *Nano Lett.* **2009**, *9*, 230–234.
4. Muller, C.; Ferenczi, T. A. M.; Campoy-Quiles, M.; Frost, J. M.; Bradley, D. D. C.; Smith, P.; Stingelin-Stutzmann, T.; Nelson, J. Binary Organic Photovoltaic Blends: A Simple Rationale for Optimum Compositions. *Adv. Mater.* **2008**, *20*, 3510–3515.
5. Kim, Y.; Cook, S.; Tuladhar, S. M.; Choulis, S. A.; Nelson, J.; Durrant, J. R.; Bradley, D. D. C.; Giles, M.; Mcculloch, I.; Ha, C. S.; *et al.* A Strong Regioregularity Effect in Self-Organizing Conjugated Polymer Films and High-Efficiency Polythiophene: Fullerene Solar Cells. *Nat. Mater.* **2006**, *5*, 197–203.
6. Li, G.; Shrotriya, V.; Huang, J.; Yao, Y.; Moriarty, T.; Emery, K.; Yang, Y. High-Efficiency Solution Processable Polymer Photovoltaic Cells by Self-Organization of Polymer Blends. *Nat. Mater.* **2005**, *4*, 864–868.
7. Ma, W.; Yang, C.; Gong, X.; Lee, K.; Heeger, A. J. Thermally Stable, Efficient Polymer Solar Cells with Nanoscale Control of the Interpenetrating Network Morphology. *Adv. Funct. Mater.* **2005**, *15*, 1617–1622.
8. van Bavel, S. S.; Sourty, E.; de With, G.; Loos, J. Three-Dimensional Nanoscale Organization of Bulk Heterojunction Polymer Solar Cells. *Nano Lett.* **2009**, *9*, 507–513.
9. Chiu, M. Y.; Jeng, U.; Su, M. S.; Wei, K. H. Morphologies of Self-Organizing Regioregular Conjugated Polymer/Fullerene Aggregates in Thin Film Solar Cells. *Macromolecules* **2010**, *43*, 428–432.
10. Chiu, M. Y.; Jeng, U.; Su, C. H.; Liang, K. S.; Wei, K. H. Simultaneous Use of Small- and Wide-Angle X-ray Techniques To Analyze Nanometer Scale Phase Separation in Polymer Heterojunction Solar Cells. *Adv. Mater.* **2008**, *20*, 2573–2578.
11. Kennedy, R. D.; Ayzner, A. L.; Wanger, D. D.; Day, C. T.; Halim, M.; Khan, S. I.; Tolbert, S. H.; Schwartz, B. J.; Rubin, Y. Self-Assembling Fullerenes for Improved Bulk-Heterojunction Photovoltaic Devices. *J. Am. Chem. Soc.* **2008**, *130*, 17290–17292.
12. Szarko, J. M.; Guo, J.; Liang, Y.; Lee, B.; Rolczynski, B. S.; Strzalka, J.; Xu, T.; Loser, S.; Marks, T. J.; Yu, L.; *et al.* When Function Follows Form: Effects of Donor Copolymer Side Chains on Film Morphology and BHJ Solar Cell Performance. *Adv. Mater.* **2010**, *22*, 5468–5472.
13. Chen, D.; Nakahara, A.; Wei, D.; Nordlund, D.; Russell, T. P. P3HT/PCBM Bulk Heterojunction Organic Photovoltaics: Correlating Efficiency and Morphology. *Nano Lett.* **2011**, *11*, 516–567.
14. Kiel, J. W.; Eberle, A. P. R.; Mackay, M. E. Nanoparticle Agglomeration in Polymer-Based Solar Cells. *Phys. Rev. Lett.* **2010**, *105*, 168701.
15. Shin, M.; Kim, H.; Park, J.; Nam, S.; Heo, K.; Ree, M.; Ha, C.-S.; Kim, Y. Abrupt Morphology Change upon Thermal Annealing in Poly(3-Hexylthiophene)/Soluble Fullerene Blend Films for Polymer Solar Cells. *Adv. Funct. Mater.* **2010**, *20*, 748–754.
16. Verploegen, E.; Mondal, R.; Bettinger, C. J.; Sok, S.; Toney, M. F.; Bao, Z. Effects of Thermal Annealing upon the Morphology of Polymer–Fullerene Blends. *Adv. Funct. Mater.* **2010**, *20*, 3519–3529.

17. Renaud, G.; Lazzari, R.; Leroy, F. Probing Surface and Interface Morphology with Grazing Incidence Small Angle X-ray Scattering. *Surf. Sci. Rep.* **2009**, *64*, 255–380.
18. Chen, S. H.; Sheu, E. Y.; Kalus, J.; Hoffmann, H. Small-Angle Neutron Scattering Investigation of Correlations in Charged Macromolecular and Supramolecular Solutions. *J. Appl. Crystallogr.* **1988**, *21*, 751–769.
19. Debye, P., Jr.; Anderson, H. R.; Brumberger, H. Scattering by an Inhomogeneous Solid. II. The Correlation Function and Its Application. *J. Appl. Phys.* **1957**, *28*, 679–683.
20. Chen, C.-Y.; Chan, S.-H.; Li, J.-Y.; Wu, K.-H.; Chen, H.-L.; Chen, J.-H.; Huang, W.-Y.; Chen, S.-A. Formation and Thermally-Induced Disruption of Nanowhiskers in Poly(3-hexylthiophene)/Xylene Gel Studied by Small-Angle X-ray Scattering. *Macromolecules* **2010**, *43*, 7305–7311.
21. Lin, J.-M.; Lin, T.-L.; Jeng, U.; Zhong, Y.-J.; Yeh, C.-T.; Chen, T.-Y. Fractal Aggregates of the Pt Nanoparticles Synthesized by the Polyol Process and Poly(*N*-vinyl-2-pyrrolidone) Reduction. *J. Appl. Crystallogr.* **2007**, *40*, s540–543.
22. Milanesio, M.; Artioli, G.; Gualtieri, A. F.; Palin, L.; Lamberti, C. Template Burning Inside TS-1 and Fe-MFI Molecular Sieves: An *In Situ* XRPD Study. *J. Am. Chem. Soc.* **2003**, *125*, 14549–14558.
23. Grandjean, D.; Beale, A. M.; Petukhov, A. V.; Weckhuysen, B. M. Unraveling the Crystallization Mechanism of CoAPO-5 Molecular Sieves under Hydrothermal Conditions. *J. Am. Chem. Soc.* **2005**, *127*, 14454–14465.
24. Bruna, P.; Crespo, D.; González-Cinca, R.; Pineda, E. On the Validity of Avrami Formalism in Primary Crystallization. *J. Appl. Phys.* **2006**, *100*, 054907–054917.
25. Allen, J. L.; Jow, T. R.; Wolfenstine, J. Kinetic Study of the Electrochemical $FePO_4$ to $LiFePO_4$ Phase Transition. *Chem. Mater.* **2007**, *19*, 2108–2111.
26. Vaynzof, Y.; Kabra, D.; Zhao, L.; Chua, L. L.; Steiner, U.; Friend, R. H. Surface-Directed Spinodal Decomposition in Poly[3-hexylthiophene] and C61-Butyric Acid Methyl Ester Blends. *ACS Nano* **2011**, *5*, 329–336.
27. Malik, S.; Jana, T.; Nandi, A. K. Thermoreversible Gelation of Regioregular Poly(3-hexylthiophene) in Xylene. *Macromolecules* **2001**, *34*, 275–282.
28. Mihailetchi, V. D.; Xie, H.; de Boer, B.; Koster, L. J. A.; Blom, P. W. M. Charge Transport and Photocurrent Generation in Poly(3-hexylthiophene): Methanofullerene Bulk-Heterojunction Solar Cells. *Adv. Funct. Mater.* **2006**, *16*, 699–708.
29. Shrotriya, V.; Yao, Y.; Li, G.; Yanga, Y. Effect of Self-Organization in Polymer/Fullerene Bulk Heterojunctions on Solar Cell Performance. *Appl. Phys. Lett.* **2006**, *89*, 063505–063507.
30. Kim, J. Y.; Frisbie, C. D. Correlation of Phase Behavior and Charge Transport in Conjugated Polymer/Fullerene Blends. *J. Phys. Chem. C* **2008**, *112*, 17726–17736.
31. Kiel, J. W.; Kirby, B. J.; Majkrzak, C. F.; Maranvillec, B. B.; Mackay, M. E. Nanoparticle Concentration Profile in Polymer-Based Solar Cells. *Soft Matter* **2010**, *6*, 641–646.
32. Parnell, A. J.; Dunbar, A. D. F.; Pearson, A. J.; Staniec, P. A.; Dennison, A. J. C.; Hamamatsu, H.; Skoda, M. W. A.; Lidzey, D. G.; Jones, R. A. L. Depletion of PCBM at the Cathode Interface in P3HT/PCBM Thin Films as Quantified *via* Neutron Reflectivity Measurements. *Adv. Mater.* **2010**, *22*, 2444–2447.
33. Treat, N. D.; Brady, M. A.; Smith, G.; Toney, M. F.; Kramer, E. J.; Hawker, C. J.; Chabinyc, M. L. Interdiffusion of PCBM and P3HT Reveals Miscibility in a Photovoltaically Active Blend. *Adv. Energy Mater.* **2011**, *1*, 82–89.
34. Watkins, P. K.; Walker, A. B.; Verschoor, G. L. B. Dynamical Monte Carlo Modelling of Organic Solar Cells: the Dependence of Internal Quantum Efficiency on Morphology. *Nano Lett.* **2005**, *5*, 1814–1818.
35. Inigo, A. R.; Chiu, H.-C.; Fann, W.; Huang, Y.-S.; Jeng, U.; Lin, T.-L.; Hsu, C.-H.; Peng, K.-Y.; Chen, S.-A. Disorder Controlled Hole Transport in MEH-PPV. *Phys. Rev. B* **2004**, *69*, 075201–075208.
36. Bässler, H. Charge Transport in Disordered Organic Photoconductors a Monte Carlo Simulation Study. *Phys. Status Solidi B* **1993**, *175*, 15–56.
37. Lan, Y.-K.; Huang, C.-I. A Theoretical Study of the Charge Transfer Behavior of the Highly Regioregular Poly(3-hexylthiophene) in the Ordered State. *J. Phys. Chem. B* **2008**, *112*, 14857–14862.
38. Lan, Y.-K.; Huang, C.-I. Charge Mobility and Transport Behavior in the Ordered and Disordered States of the Regioregular Poly(3-hexylthiophene). *J. Phys. Chem. B* **2009**, *113*, 14555–14564.
39. Agostinelli, T.; Lilliu, S.; Labram, J. G.; Campoy-Quiles, M.; Hampton, M.; Pires, E.; Rawle, J.; Bikondoa, O.; Bradley, D. D. C.; Anthopoulos, T. D.; *et al.* Real-Time Investigation of Crystallization and Phase-Segregation Dynamics in P3HT:PCBM Solar Cells During Thermal Annealing. *Adv. Funct. Mater.* **2011**, *21*, 1701–1709.
40. Jeng, U.; Su, C.-H.; Su, C.-J.; Liao, K.-F.; Chuang, W.-T.; Lai, Y.-H.; Chang, Y.-J.; Chen, Y.-J.; Huang, Y.-S.; Lee, M.-T.; *et al.* A Small/Wide-Angle X-ray Scattering Instrument for Structural Characterization of Air–Liquid Interfaces, Thin Films and Bulk Specimens. *J. Appl. Crystallogr.* **2010**, *43*, 110–121.
41. Yagi, N.; Inoue, K. CMOS Flat Panel Detectors for SAXS/WAXS Experiments. *J. Appl. Crystallogr.* **2007**, *40*, s439–s441.
42. Hsu, C.-H.; Jeng, U.; Lee, H.-Y.; Windover, D.; Lu, T.-M. Structural Study of a Low Dielectric Thin Film Using X-ray Reflectivity and Grazing Incidence Small Angle X-ray Scattering. *Thin Solid Films* **2005**, *472*, 323–327.
43. Mihailetchi, V. D.; Wildeman, J.; Blom, P.W. M. Space-Charge Limited Photocurrent. *Phys. Rev. Lett.* **2005**, *94*, 126602–126605.
44. Melzer, C.; Koop, E. J.; Mihailetchi, V. D.; Blom, P. W. M. Hole Transport in Poly(phenylene vinylene)/Methanofullerene Bulk-Heterojunction Solar Cells. *Adv. Funct. Mater.* **2004**, *14*, 865–870.
45. Chen, S.-H.; Lin, T.-L. In *Methods of Experimental Physics—Neutron Scattering in Condensed Matter Research*; Sköld, K., Price, D. L., Eds.; Academic Press: New York, 1987; Vol. 23B, Chapter 16.
46. Sheu, E. Y. Polydispersity Analysis of Scattering Data from Self-Assembled Systems. *Phys. Rev. A* **1992**, *45*, 2428–2438.
47. Hayter, J. B.; Penfold, J. An Analytic Structure Factor for Macroion Solutions. *Mol. Phys.* **1981**, *42*, 109–118.
48. Su, C. H.; Jeng, U.; Chen, S. H.; Lin, S. J.; Wu, W. R.; Chuang, W.-T.; Tsai, J. C.; Su, A. C. Nanograin Evolution in Cold Crystallization of Syndiotactic Polystyrene as Illustrated *via In-Situ* Small/Wide-Angle X-ray Scattering and Differential Scanning Calorimetry. *Macromolecules* **2009**, *42*, 6656–6664.